Supplementary information

Modeling galvanostatic charge-discharge of nanoporous supercapacitors

Liang Zeng[1], Taizheng Wu[1], Ting Ye[1], Tangming Mo[1], Rui Qiao[2], and Guang Feng[1,*]

Table of Contents

[1]State Key Laboratory of Coal Combustion, School of Energy and Power Engineering, Huazhong University of Science and Technology (HUST), Wuhan 430074, China. [2]Department of Mechanical Engineering, Virginia Tech, Blacksburg, VA 24061, USA. E-mail: gfeng@hust.edu.cn

Part 1. Stable cycle of charging-discharging process

We modeled the galvanostatic charging-discharging process of the supercapacitor for 30 cycles. After a few cycles, it will reach stability. Supplementary Fig. 1 shows that the number density of cations near the positive electrode, obtained from GCD-CPM simulations for an open electrode system with a period of 100 ps. In this work, all the data shown in the main text is in a stable cycle by averaging the data of the last ten cycles. Hence, the time mentioned in this work refers to the time relative to the beginning of the averaged stable cycle.

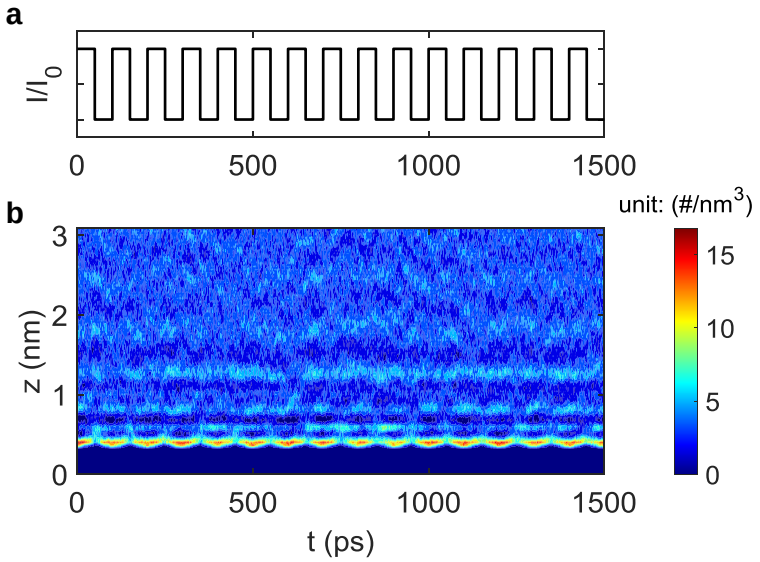

Supplementary Figure 1 | Input current and evolution of cation number density. a, Input current of galvanostatic charge-discharge. **b**, Time-evolution cation number density near positive electrodes, obtained from GCD-CPM simulations. Only the first 15 cycles are shown.

Part 2. Potential and charge on open electrodes

For GCD-CPM, the probability distribution of electrode atom charges is $f(q,t)$, which is defined as the ratio of $N(q,t)$ to the total atoms of the electrode. $N(q,t)$ refers to the number of electrode atoms with charges in the range of $q - dq/2$ and $q + dq/2$ at time *t*. We set dq as $\frac{Q_{max}-Q_{min}}{N_{bin}}$, where Q_{max} and Q_{min} are the maximum and minimum charge values of all atoms at the electrode during the charging process; N_{bin} is set as 300 here. Similarly, the probability distributions of electrode atom potentials in GCD-CCM can be obtained.

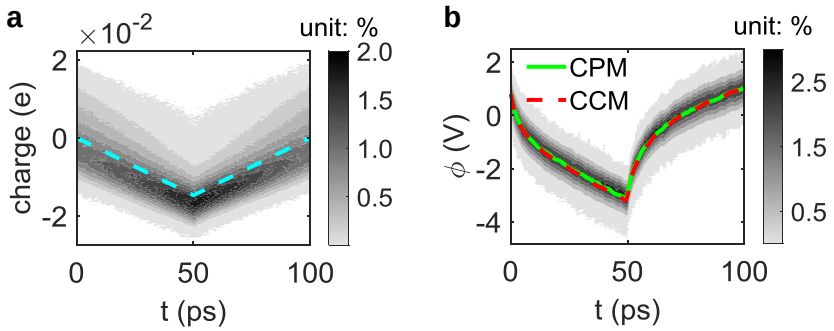

Supplementary Figure 2 | Charge and potential on electrode atoms in open electrode systems. **a,** Gray contour indicates probability distributions of negative electrode atom charges vary with time obtained from GCD-CPM simulations, and the dashed line is the average. **b**, Gray contour indicates the probability distributions of negative electrode atom potential vary with time obtained from GCD-CCM simulations. The red dashed line is the average. The solid green line is the potential of the negative electrode obtained from GCD-CPM simulations.

Part 3. Comparison of EDL structures in open electrode systems

As mentioned in the main text, the number densities of cations near the positive electrode by GCD-CPM and GCD-CCM are almost identical. For a more intuitive comparison, Supplementary Fig. 3 shows the number density of cations near the positive electrode at two moments (0 and 50 ps). Similarly, Supplementary Fig. 4 shows the number densities of cations near the negative electrode, anions near the positive electrode, and anions near the negative electrode. Supplementary Fig. 5 shows orientations of cations adsorbed on the negative electrode. As shown in Supplementary Fig. 5a, η is defined as the angle between the normal of the electrode surface and the normal of the cation plane, α is defined as the angle between the normal of the electrode surface and the vector pointing from the imidazole ring to ethyl, and β is defined as the angle between the normal of the electrode surface and vector pointing from imidazole ring to methyl. The first cation layer refers to the cations at the region between the electrode surface and the first valley of cation number density, as Supplementary Fig. 4 shows. One can find that the ion responses obtained by GCD-CPM and GCD-CCM are almost the same.

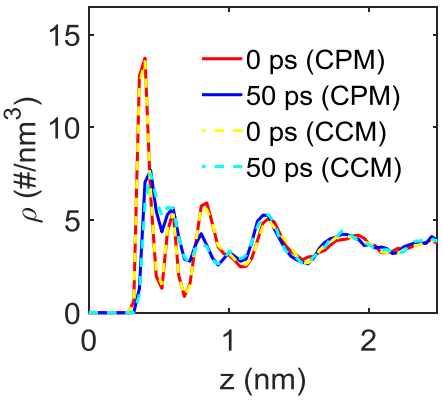

Supplementary Figure 3 | Number density of cation near positive electrode at 0 and 50 ps.

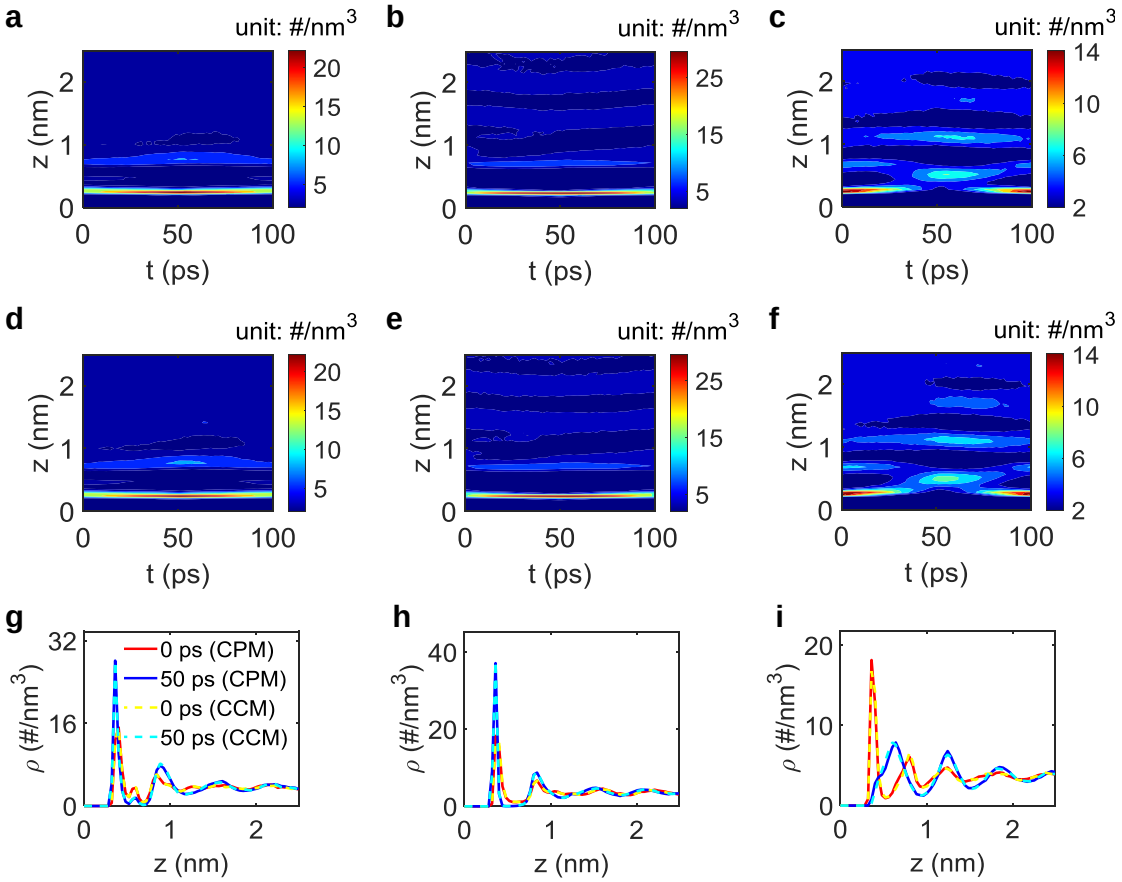

Supplementary Figure 4 | Ion number density in open electrode systems. a-c, Number density of cation near the negative electrode (**a**), anion near the positive electrode (**b**), and anion near the negative electrode (**c**) as a function of distance from electrode and time. The data obtained from GCD-CPM simulations. **d-f**, Number density of cation near the negative electrode (**d**), anion near the positive electrode (**e**), and anion near the negative electrode(**f**) as a function of distance from electrode and time. The data obtained from GCD-CCM simulations. **g-i**, Number density of cation near the negative electrode (**g**), anion near the positive electrode (**h**), and anion near the negative electrode (**i**) at time 0 and 50 ps.

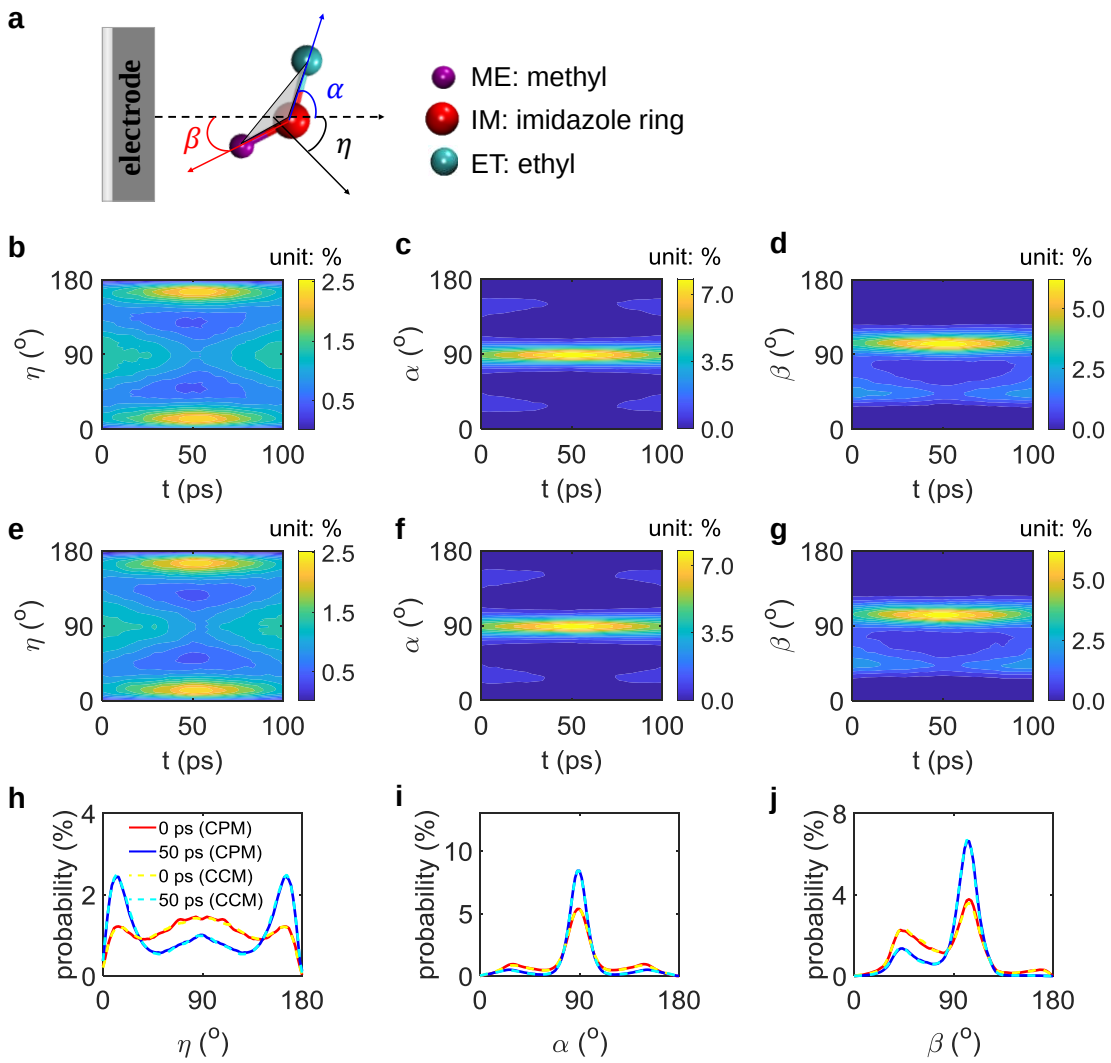

Supplementary Figure 5 | Orientation of the first cation layer adsorbed at the negative electrode of open electrode systems. a, Schematics for cation orientation. **b-d**, Probability distribution of η (**b**) α (**c**) and β (**d**) with time. The data obtained from GCD-CPM simulations. **e-g**, Probability distribution of η (**e**) α (**f**) and β (**g**) with time. The data obtained from GCD-CCM simulations. **g-i**, Probability distribution of η (**h**), α (**i**), and β (**j**) at 0 ps and 50 ps.

Part 4. Potential and charge on nanoporous electrodes

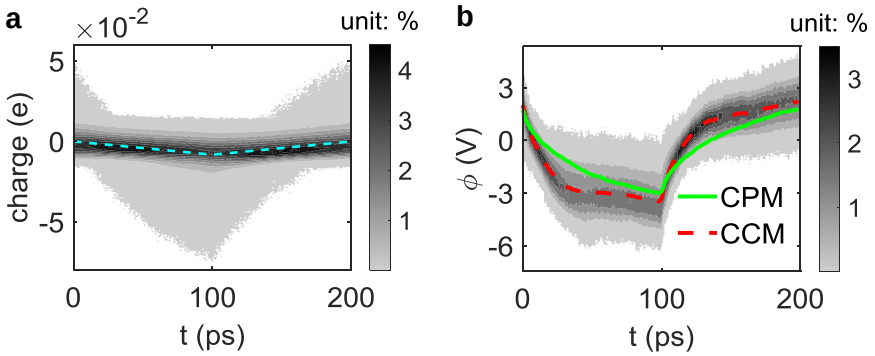

Supplementary Figure 6 | Charge and potential on electrode atoms in nanoporous electrode systems. a, Gray contour indicates probability distributions of negative electrode atom charges vary with time obtained from GCD-CPM simulations, and the dashed line is the average. **b**, Gray contour indicates the distributions of negative electrode atom potential vary with time obtained from GCD-CCM simulations, and the red dashed line is the average. The solid green line is the potential of the negative electrode obtained from GCD-CPM simulations.

Part 5. Evolution of in-pore charge density and effective diffusion

According to the mean-field theory[1, 2], the spatial and temporal distribution of charge densities inside the electrode pore ρ_e is described by the diffusion equation as

$$\frac{\partial \rho_e}{\partial t} = D_{eff} \frac{\partial \rho_e^2}{\partial^2 z}, \tag{S4}$$

where D_{eff} is the effective diffusion coefficient. Hence, D_{eff} can be calculated by minimizing the difference of in-pore charge density evolution between the molecular simulation and diffusion equation. The initial and boundary conditions used to solve the minimization problem are directly from molecular simulations. Supplementary Figures 7-8 show the evolution of in-pore charge density inside the electrode pore obtained by GCD-CPM and GCD-CCM simulations and their fitting based on the minimization problem. Supplementary Fig. 9 shows the effective diffusion inside the negative electrode pore obtained by solving the minimization problem.

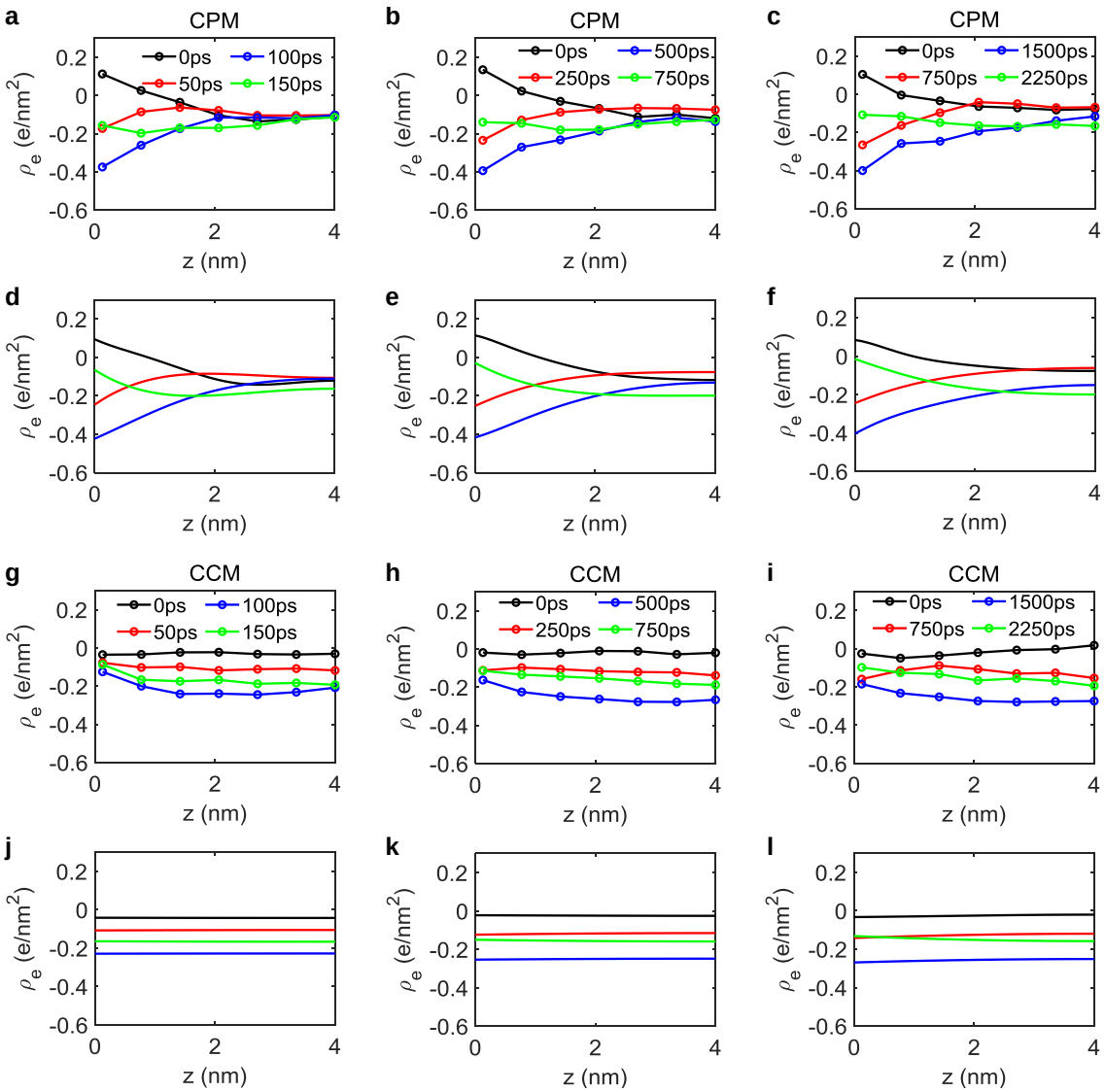

Supplementary Figure 7 | Evolution of in-pore charge density along the pore axis of the positive nanoporous electrode and corresponding fitting results. a-c, Evolution of in-pore charge density along the pore axis with the electric current period of 200 ps (**a**), 1000 ps (**b**), and 3000 ps (**c**) obtained from GCD-CPM simulations. **d-f**, The fitting in-pore charge density with the electric current period of 200 ps (**d**), 1000 ps (**e**), and 3000 ps (**f**), using GCD-CPM simulation data. **g-i**, Evolution of in-pore charge density along the pore axis with electric current periods of 200 ps (**g**), 1000 ps (**h**), and 3000 ps (**i**), obtained from GCD-CCM simulations. **j-l**, The fitting in-pore charge density with electric current periods of 200 ps (**j**), 1000 ps (**k**), and 3000 ps (**l**), using GCD-CCM simulation data.

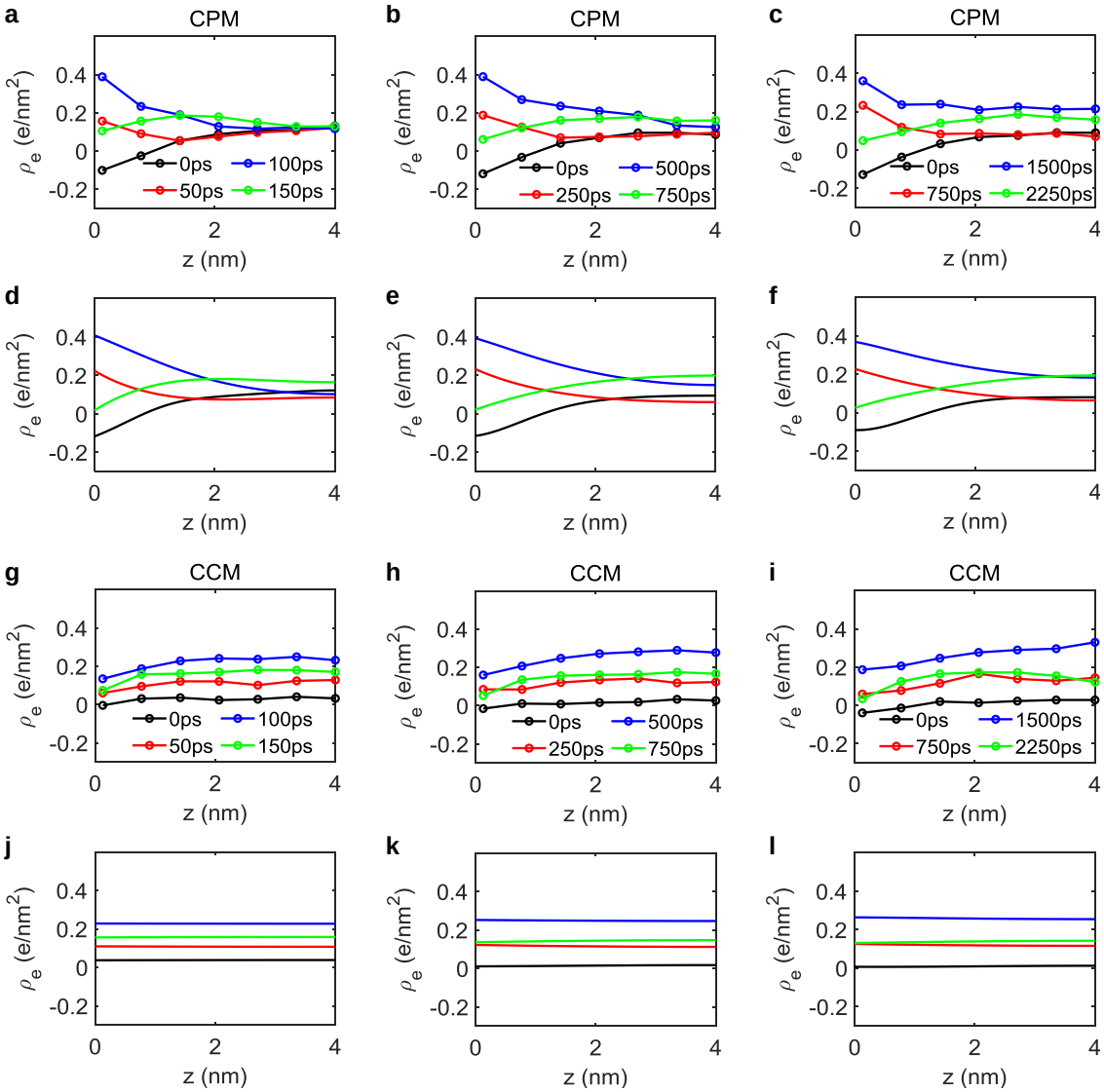

Supplementary Figure 8 | Evolution of in-pore charge density along the pore axis of the negative nanoporous electrode and corresponding fitting results. a-c, Evolution of in-pore charge density along the pore axis with the electric current period of 200 ps (**a**), 1000 ps (**b**), and 3000 ps (**c**) obtained from GCD-CPM simulations. **d-f**, The fitting in-pore charge density with the electric current period of 200 ps (**d**), 1000 ps (**e**), and 3000 ps (**f**), using GCD-CPM simulation data. **g-i**, Evolution of in-pore charge density along the pore axis of the electric current period of 200 ps (**g**), 1000 ps (**h**), and 3000 ps (**i**), obtained from GCD-CCM simulations. **j-l**, The fitting in-pore charge density with the electric current period of 200 ps (**j**), 1000 ps (**k**), and 3000 ps (**l**), using GCD-CCM simulation data.

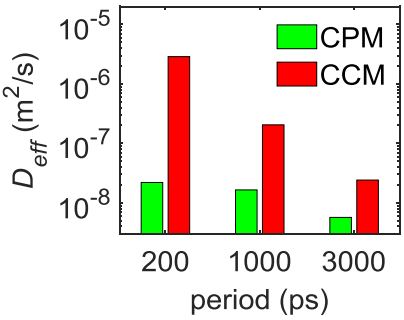

Supplementary Figure 9 | Effective diffusivity inside the negative electrode pore.

Part 6. Comparison of heat generation of nanoporous systems

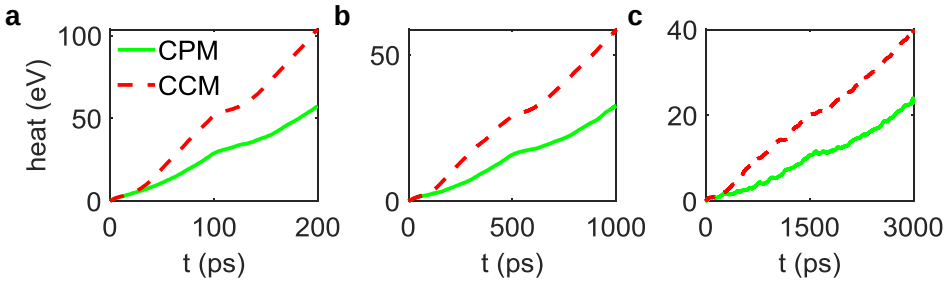

Supplementary Figure 10 | Evolution of heat generation in nanoporous electrode systems. **a-c,** Electric current periods are 200 ps (**a**), 1000 ps (**b**), and 3000 ps (**c**).

Part 7. Experimental detail and validation of molecular modeling

Materials for experiment

Commercial activated carbon cloth ACC-5092-15 was purchased from Kynol, fabricated into the free-standing and binder-free electrode. Before use, it was dried at 120 ℃ under vacuum for 12 hours. The ionic liquid [EMIM][BF_4] (Iolitec Technologies) was purified at 85 ℃ by the Schlenk line for 24 hours.

Material characterization

Nitrogen sorption experiments were performed with an Autosorb iQ system (Quantachrome) at 77 K. The ACC was degassed at 10^{-2} Pa at a temperature of 200 ℃ for 10 hours. The sample was found to exhibit a gravimetric BET surface area of 1534 m^2/g. The pore size analysis was calculated (Supplementary Fig. 11) using quenched-solid density functional theory (QSDFT), assuming a slit-shaped pore model. The average pore size of micropores is calculated as ~0.72 nm on the basis of volume-weighted pore size d_{50}.

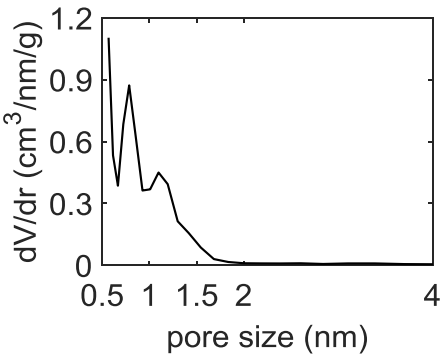

Supplementary Figure 11 | Pore size distribution of porous carbons. The carbon is ACC-5092-15, and the pore size is calculated by applying quenched-solid density functional theory (QSDFT), assuming a slit-shaped pore model.

Assembly and instrumentation

Before fabrication, two 10mm-diameter ACC electrodes were soaked into a 10 mL glass vial filled with [EMIM][BF_4] in an argon-filled glove box containing less than 0.01 ppm H_2O and O_2. Then a two-electrode electrochemical cell was fabricated in the same glove box. After the addition of the electrolyte, the electrochemical cells were

hermetically sealed and transferred out of the glove box. Electrochemical measurements were performed on a CS-350H workstation from Wuhan Corrtest Instrument Co. Ltd.

Electrochemical measurement

For comparison with modeling, the galvanostatic charge-discharge tests were carried out for our cell. The setting time of charging and discharging is equal, which is not the regular set with voltage limitation. A series of electric currents with different charge-discharge periods (12 to 400 s) were adopted to figure out the same dimensionless period with simulation. Supplementary Fig. 12 shows GCD curves obtained in the experiment, and their dimensionless periods are equal with the GCD-CPM simulations. Their actual periods are 20, 260, and 360 s. To compare with modeling, the IR drops, mainly caused by the electrode resistance[3-5] and not reflected in simulations, are removed from the experimental GCD curve. The treated experimental curves are then compared with GCD-CPM results through the dimensionless TLM-fitted GCD curves in Supplementary Fig. 13-14.

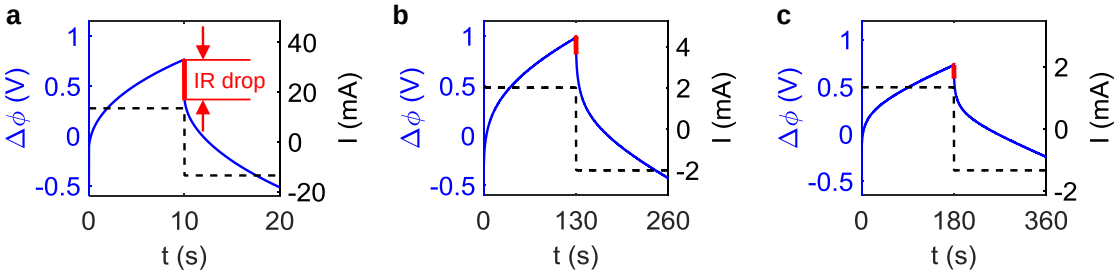

Supplementary Figure 12 | Experimental GCD curves. a-c, GCD curves obtained from experiments whose periods are 20 s (**a**), 260 s (**b**), and 360 s (**c**).

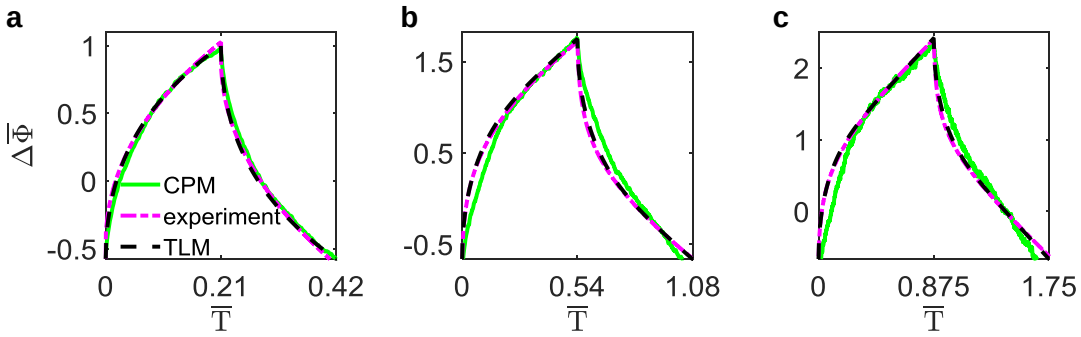

Supplementary Figure 13 | Validation of GCD-CPM by experiment. a-c, Dimensionless GCD curves obtained from GCD-CPM simulations and experiments, and their fitting by the transmission line model. The dimensionless periods are 0.42 (**a**), 1.08 (**b**), and 1.75 (**c**).

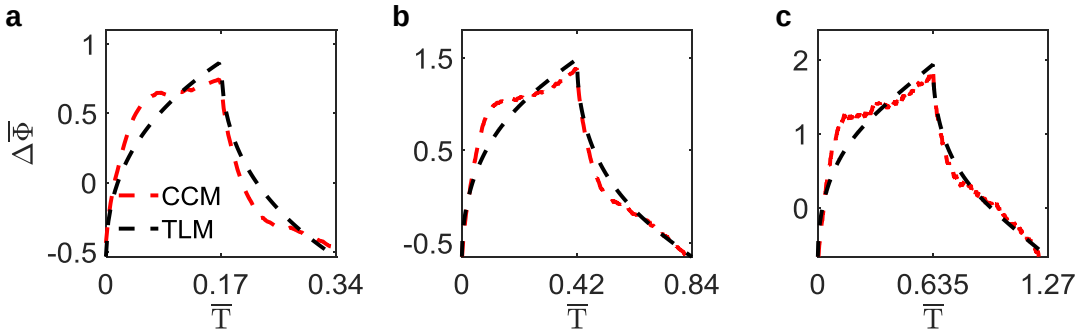

Supplementary Figure 14 | Fitting of GCD curves obtained from GCD-CCM simulations based on the dimensionless transmission line model. a-c, Dimensionless periods of 0.34 (**a**), 0.84 (**b**), and 1.27 (**c**).

Part 8. Hysteresis of ion adsorption-desorption

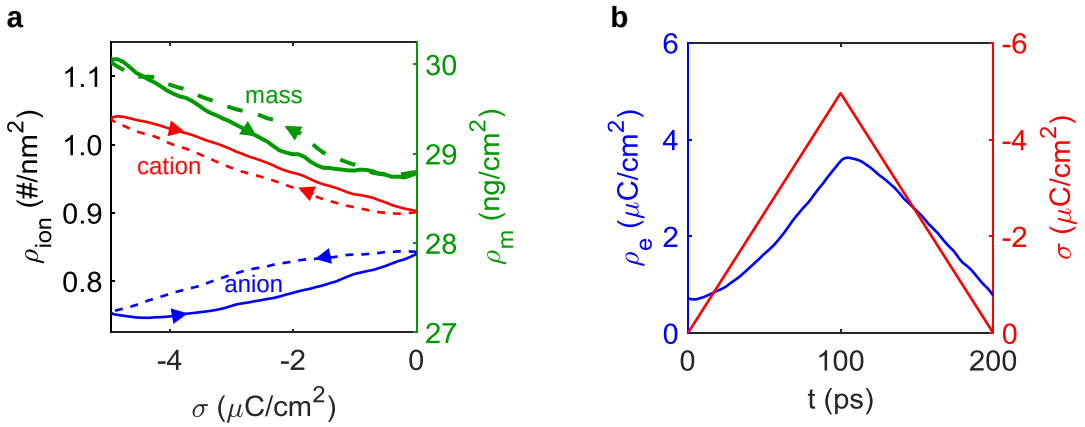

Supplementary Figure 15 | Hysteresis in the negative electrode of nanoporous electrode systems. a, Green line is the total mass density of in-pore electrolyte. Red and blue lines are the number densities of in-pore cations and anions, respectively. Solid (dashed) line is the discharging (charging) process. **b,** Blue line represents the charge density coming from in-pore ions, and red line is the charge density on the electrode. Results are for the negative electrode.

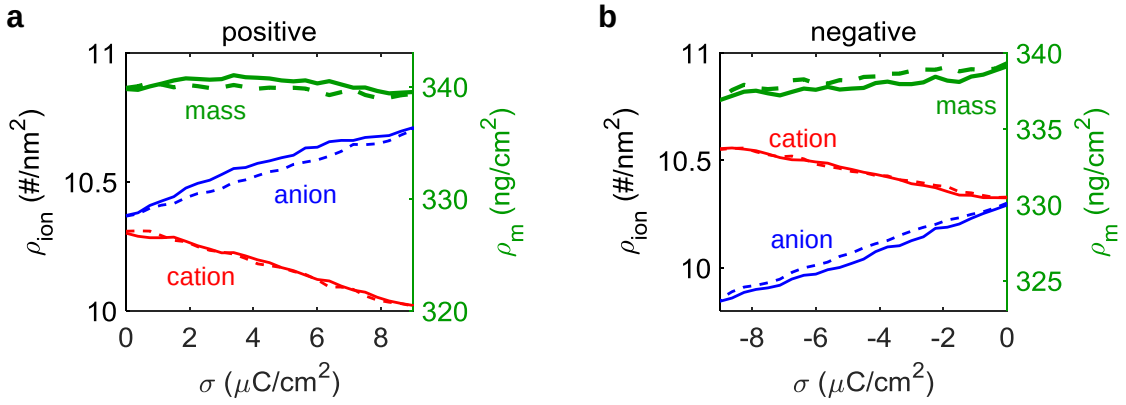

Supplementary Figure 16 | Hysteresis in open electrode systems. a-b, The average number density of cations and anions near the positive electrode (**a**) and the negative electrode (**b**). The data is from the region of 0–3 nm to the electrode surface. Green line is the total mass density from the electrolyte. Red and blue lines are the number densities of cations and anions, respectively. Solid (dashed) line is the discharging (charging) process. The electric current period is 100 ps.

Like the nanoporous electrode system, the charge from the electrolyte side changes slowly than that from the electrode side for open electrode systems. Here we explore the effect of hysteresis of ion adsorption-desorption on the GCD curves. σ_{lagging} is used to describe how the charge from the electrolyte lags behind that on the electrode, and it is defined as

$$\sigma_{\text{lagging}} = \sigma + \int_0^{L/2} \rho_e dz, \tag{S1}$$

where σ is the total surface charge density of one electrode and ρ_e is the charge density through the EDL near this electrode. L is the distance between the positive and negative electrodes.

For the open electrode systems, the potential difference between the positive and negative electrodes can be derived from charge distribution[6], as

$$\Delta\phi = \frac{\sigma}{\epsilon_0} L - \frac{1}{\epsilon_0} \int_0^L (L - z)\rho_e dz, \tag{S2}$$

where ϵ_0 is vacuum permittivity. We then divide the surface charge σ into two parts: the lagging charge σ_{lagging} and the balanced charge $\sigma - \sigma_{\text{lagging}}$. Then $\Delta\phi$ is divided consequently into

$$\Delta\phi_{\text{lagging}} = \frac{\sigma_{\text{lagging}}}{\epsilon_0} L, \tag{S3a}$$

$$\Delta\phi_{\text{rest}} = \frac{\sigma - \sigma_{\text{lagging}}}{\epsilon_0} L - \frac{1}{\epsilon_0} \int_0^L (L - z)\rho_e dz, \tag{S3b}$$

where $\Delta\phi_{\text{lagging}}$ is produced only by σ_{lagging}, and $\Delta\phi_{\text{rest}}$ is produced by $\sigma - \sigma_{\text{lagging}}$. The degree of charge lagging decreases as P increases (Supplementary Fig. 17a), since electrolyte ions require a longer time to respond to the electrode polarization. The asymmetry and the negative values of the GCD curve are caused by such lagging charge, as shown in Supplementary Fig. 17b.

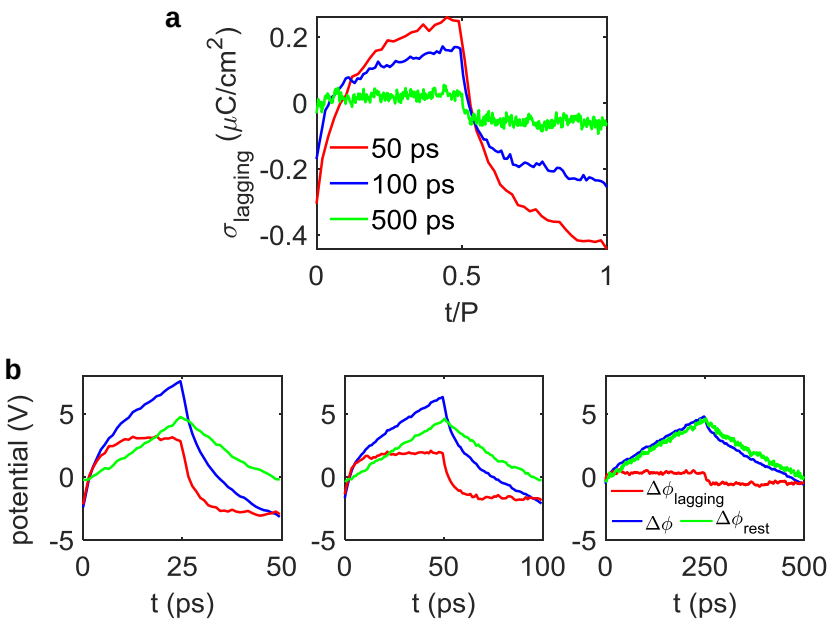

Supplementary Figure 17 | Charge lagging and its effect on GCD curves for open electrode systems. a, Evolution of lagging charge σ_{lagging}. **b,** Evolution of $\Delta\phi$, $\Delta\phi_{\text{lagging}}$, and $\Delta\phi_{\text{rest}}$.

Supplementary References

1. Kondrat S., Wu P., Qiao R., Kornyshev A. A. Accelerating charging dynamics in subnanometre pores. *Nature Materials* 2014, 13(4)**:** 387-393.
2. Kondrat S., Kornyshev A. Charging dynamics and optimization of nanoporous supercapacitors. *The Journal of Physical Chemistry C* 2013, 117(24)**:** 12399-12406.
3. Noori A., El-Kady M. F., Rahmanifar M. S., Kaner R. B., Mousavi M. F. Towards establishing standard performance metrics for batteries, supercapacitors and beyond. *Chemical Society Reviews* 2019, 48(5)**:** 1272-1341.
4. Gonz âez A., Goikolea E., Barrena J. A., Mysyk R. Review on supercapacitors: Technologies and materials. *Renewable and Sustainable Energy Reviews* 2016, 58**:** 1189-1206.
5. Burke A., Miller M. Testing of electrochemical capacitors: Capacitance, resistance, energy density, and power capability. *Electrochimica Acta* 2010, 55(25)**:** 7538-7548.
6. Feng G., Zhang J. S., Qiao R. Microstructure and capacitance of the electrical double layers at the interface of ionic liquids and planar electrodes. *The Journal of Physical Chemistry C* 2009, 113(11)**:** 4549-4559.